# Overpressure Contact Printing and Its Applications in the Fabrication of Arrays of Magnetic Rings

The elastomeric property of poly(dimethylsiloxane) (PDMS) allows stamps made of this polymer to be widely used in replicating patterns with high fidelity through the conformal contact between the substrate and the stamp surfaces.[1–3] This unique property is also the origin of stamp deformations. Although the conformal contact is preferred in contact printing, the application of stamp deformations in nanofabrication is severely under investigated. Xia *et al*. were able to create patterns with size-reduced features by intentionally applying external forces to laterally deform the stamps during contact printing.[4] This article shows that not only can size reductions be achieved by applying pressure normal to the substrates during contact printing, but also new patterns different from those features on the stamps can be generated by this patterning approach. This method is referred to as overpressure contact printing (oCP). It is particularly worthwhile to mention that oCP is unique in the fabrication of new features while having the advantage of miniaturization.

As indicated, overpressure contact printing relies on the deformation of PDMS stamps. The mechanical properties of PDMS and the behaviors of PDMS stamps have been examined recently.[5,6] Delamarche *et al*. showed that the height-to-width ratios—the aspect ratios—of the relief structures on PDMS stamps need to be between about 0.2 and 2 in order to obtain defect-free printing. If the aspect ratio of the PDMS feature is too high, the roof of the feature may come into contact with a substrate under its own weight or under an external pressure. When the aspect ratios are too low, the relief structures are not able to withstand the stamp weight. The compressive forces of printing and the adhesion force between the stamp and the substrate can both cause the similar result.[5,7,8] This article will briefly describe the theoretical analysis of this deformation of PDMS.[8]

Figure 99.84(a) shows a basic geometry of a stamp that consists of periodic relief line features with height of $h$, feature width of $2w$, and trench width of $2a$. When pressure is applied to the stamp, several deformations occur, including in-plane lateral expansion, "sagging" of the trench, and relief feature from compression by the external stress. The in-plane expansion of the stamp could be minimized if a stiff backplane such as a glass plate on the elastomer is used since the Young's modulus of glass is much greater than that of PDMS. Because the strength of stress applied is typically of the order of the Young's modulus of PDMS, the Poisson expansion of the stamp bonded to the glass backplane can be several orders of magnitude lower than that of a stamp without a backplane and negligible.[8]

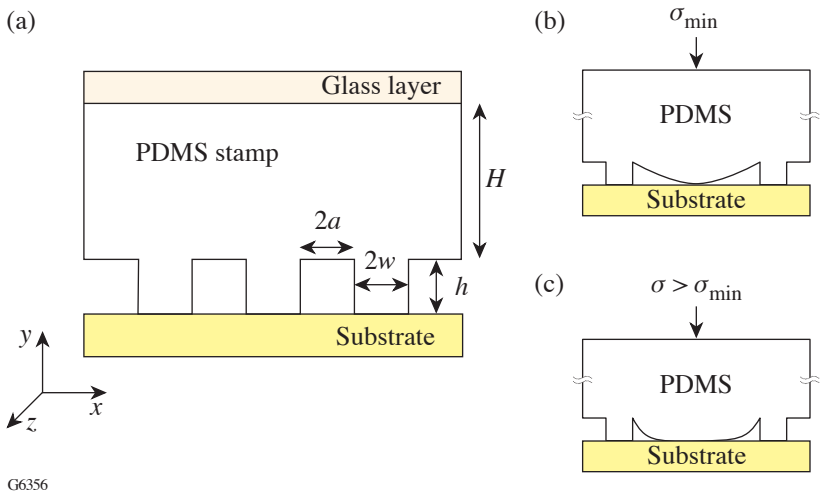


Figure 99.84
Illustrations of (a) the basic geometry of a PDMS stamp and stamps deformed into contact with substrates under (b) required minimum and (c) excess pressures.

Most elastomers are rubber elastic and incompressible with Poisson's ratio $v$ of approximately 0.5. The Young's modulus of PDMS depends strongly on the mixing ratios between prepolymer precursor and curing agent and the preparation conditions, such as curing time and temperature. The Young's modulus (E) and density of the PDMS material with different mixing ratios have been studied by examining the deflection of a single-side clamped PDMS cantilever beam.[6] To keep the mechanical properties of the PDMS consistent, a mixing ratio of 10:1 between the polymer and curing agent was used along with a curing temperature of 70°C overnight for all the stamps tested in this work. The Young's modulus of PDMS stamps prepared at these conditions is ~0.75 MPa as indicated by Armani *et al*.[6] For a qualitative analysis, the height of the stamp backbone is neglected because it is normally much greater than the height of the relief features, and the amount of pressure from the weight of the stamp is negligible as compared to the amount of pressure applied. With these assumptions, the model for promoted contact between the roof and substrates under external stress [Fig. 99.84(b)] can be simplified as follows:[8]

$$V_{\max} = \frac{4\sigma_{\min}}{\pi E^*}(w+a)\cosh^{-1}\left\{\sec\left[\frac{w\pi}{2(w+a)}\right]\right\}, \qquad (1)$$

where $V_{\max}$ is the maximum displacement of the roof by an applied minimum external stress $\sigma_{\min}$ and $E^* = E\Big/\left(1-v^2\right)$. All variables in the equation are known except external stress $\sigma$, which can be varied to give different degrees of contacts between the roof and the substrate [Fig. 99.84(c)].

This article further demonstrates the application of the oCP technique in creating FePt magnetic ring and anti-ring structures from microwell patterns of $Pt@Fe_2O_3$ nanoparticles. We are particularly interested in making arrays of these magnetic structures because such patterns are candidates for magnetic random access memory (MRAM).[9] In MRAM, it requires a reproducible switching mechanism from one cycle to the next. In this context, flux closure magnetic elements are favorable as compared to linear magnetic elements because of less dependence on the edge domain effect. For linear elements, the randomly magnetized edge domains form at the flat edges, which can prevent repeatable magnetic switching. On the contrary, the circular disks and rings with flux closure magnetization are more sustainable to edge roughness and, therefore, are suitable for device fabrication. In magnetic disks, however, a center vortex can form, and vortex displacement may lead to an irreproducible switching. A ring-shaped magnetic element can form a stable flux closure magnetization without the central vortex because of the geometry confinement of the ring.[9] A vertical magnetoresistive random access memory based on ring elements has been proposed recently.[9]

Nano-rings have been fabricated by *e*-beam lithography or nanoimprinting.[10–12] Although *e*-beam lithography can create ordered arrays of nano-rings with controllable diameter and thickness, the process is usually cumbersome and inaccessible to the majority of researchers. More recently, Scott *et al*. have successfully fabricated ordered arrays of magnetic rings by using controlled dewetting of polymeric percursors.[13] This technique is versatile and able to create ordered ring arrays of iron- and cobalt-containing polymers. Upon thermal treatment, the polymers can decompose and form magnetic ceramics. The combined dewetting and pyrolysis processes tend to lead, however, to the formation of local organization of the magnetic nanoparticles within the bands, while the continuity is pivotal for the rings to exhibit the unique flux closure magnetization mode. Here, an alternative technique to fabricate nano-rings in a controlled fashion using oCP is presented. The capability of the oCP technique is illustrated using self-assembled monolayers (SAM) on gold. The application of this method in making arrays of FePt rings from pLB films[14] of 4-nm $Pt@Fe_2O_3$ core–shell nanoparticles[15] is then described.

Gold substrates used in this research were made by depositing a 45-nm-thick gold layer onto silicon wafers using an *e*-beam evaporator. The ink was hexadecanethiol in an ethanol solution (~1 mM).[2] The PDMS patterns were replicated from photoresist (Shipley 1813) patterns on silicon following the standard procedures.[16] The height of the photoresist features made from this photoresist is expected to be 1.3 $\mu$m and was examined using a tapping-mode atomic force microscope (AFM, Digital Instrument, Nanoscope IIIa). In a typical procedure, the gold substrates and stamps were first cleaned with ethanol and dried under a stream of $N_2$ gas. A small amount of ink solution was then applied on the stamp surface using a cotton tip. The excess thiol solution was washed away with ethanol and dried with $N_2$ gas for 2 min. The stamp was then placed in contact with the gold substrate. To ensure conformal contact between the stamp and the substrate, and contact between the roof of the features and the substrate surface, pressure (~0.3 MPa) was applied normal to the substrate surface by using an iron block (3.2 kg/cm$^2$) during printing. The size of the stamp was typically $1 \times 1$ cm$^2$. The unprotected gold regions were removed by an aqueous etching solution consisting of $K_3Fe(CN)_6$ (0.01 M), $K_4Fe(CN)_6$ (0.001 M), $K_2S_2O_3$ (0.1 M), and KOH (1 M). The optimized duration for etching away 45 nm of gold was about 8.5 min. The etched

substrates were washed thoroughly with ethanol and deionized water and dried with $N_2$.

The ability to pattern $\gamma$-$Fe_2O_3$ (Ref. 17) and $Pt@Fe_2O_3$ nanoparticles[15,18] using the patterned Langmuir–Blodgett (pLB) technique[14,15] has been demonstrated. Both monolayer and multilayer depositions of nanoparticles are possible using the pLB technique through a layer-by-layer approach. This pLB technique has been used to pattern $Pt@Fe_2O_3$ core–shell nanoparticle arrays of rings and anti-rings in conjunction with oCP. The experimental procedure is shown in Fig. 99.85. In a typical procedure of making nanoparticle patterns, designed multilayers of Langmuir films of ~4-nm $Pt@Fe_2O_3$ nanoparticles were transferred onto a PDMS stamp of microwell pattern (10 $\mu$m). The nanoparticle-coated stamp was then contact printed on a plasma-cleaned Si wafer at a pressure of ~0.3 MPa for 2–3 s. The initial printing (oCP) generated the anti-ring pattern of nanoparticles [Fig. 99.85(a)], while removing the particles from the centers of the roofs of the wells that made contact with the substrate. The stamp was then carefully released from the substrate and used for a second printing under a pressure of ~0.3 MPa and a stamping time of 10 s. Arrays of ring structures could be obtained from the second printing, which is referred to as extended oCP [Fig. 99.85(b)].

Field-emission SEM images were obtained using a LEO 982 microscope. Tapping-mode AFM and magnetic-force microscope (MFM) images were collected using a Digital Instrument Nanoscope IIIa microscope. The magnetic tips (MFMR) were purchased from Nanosensors. The cantilevers are coated with cobalt alloy (40 nm thick) on the tip side and aluminum (30 nm thick) on the detector side. The tip radii are typically less than 50 nm. The tips are magnetized using a permanent magnet (field strength: ~0.2 Tesla) prior to MFM imaging. MFM images were obtained using the interleave mode at a lift scan height of 50 nm.

To demonstrate the oCP technique, gold microstructures were created on silicon starting from SAM of thiolate on gold surfaces. In this case, the SAM acted as an etching resist layer. Several line patterns with various height/width aspect ratios have been tested. The physical dimensions and their corresponding aspect ratios of some of the relief line patterns on the PDMS stamps used in this project are listed in Table 99.V. These numbers have been obtained from SEM and AFM characterizations of the photoresist masters and the PDMS stamps (Fig. 99.86). In oCP, the roof of the stamp is intentionally deformed to promote the contact with the substrate [Fig. 99.84(b)]. The minimum amount of pressure $\sigma_{min}$ required to make the initial contact between the roof of the stamp

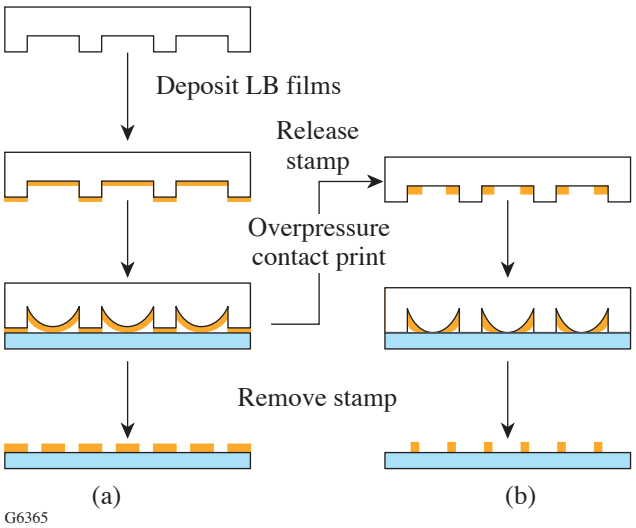


Figure 99.85
The experimental procedure for (a) overpressure and (b) extended overpressure contact printing.

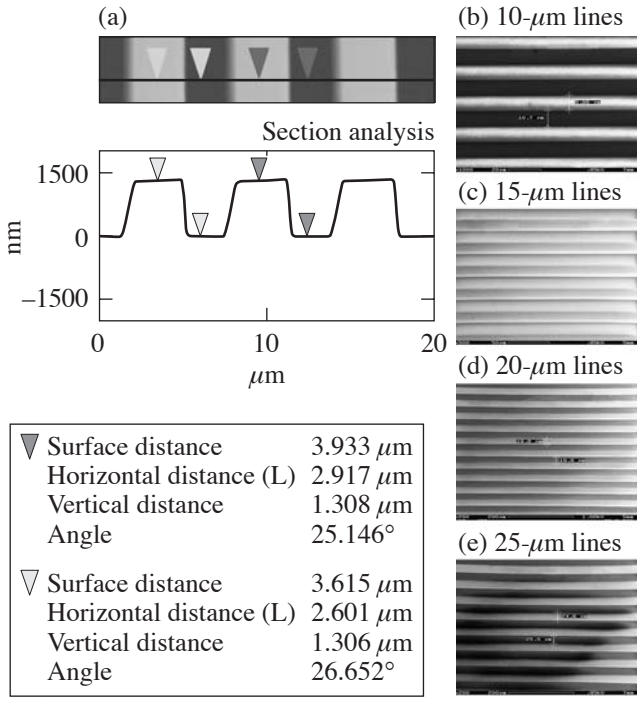


Figure 99.86
(a) AFM images and cross-section analyses showing the height (1.3 $\mu$m) of the PDMS stamps used in this work and [(b)–(e)] the SEM images of the photoresist masters of line patterns (10, 15, 20, and 25 $\mu$m) used in this study.

and the substrate was estimated for each of the stamps used based on the equation and data presented above; the results are listed in Table 99.V. The minimum pressures needed for the various stamps used were all below the Young's modulus of PDMS made at the current synthetic conditions (0.75 MPa)[6] and the amount of pressure applied (0.3 MPa). By applying pressure greater than the minimum, a higher degree of deformation can be obtained [Fig. 99.84(c)].

Figure 99.87 shows a series of SEM images of etched trenches on gold substrates fabricated by the oCP technique using the equally spaced line stamps presented in Table 99.V. The etched patterns consisted of arrays of gold lines separated by fine trenches (insets of Fig. 99.87). It is noticeable that the trenches between these lines were slightly uneven in width. This is most likely due to the unevenness of the weight when situated on top of the stamp. The contrast in SEM images of gold on silicon could also vary slightly. The light and dark line structures shown in Figs. 99.87(a) and 99.87(d) on both sides of the trenches were Au substrates resulting from the different etching resistance from the SAM's. During the initial oCP, the stamp was placed in intimate contact with the substrate where only the protruded structures on the stamp were able to contact the substrate [the lighter lines in Figs. 99.87(a) and 99.87(d)]. The roofs of the stamps were then brought into contact with the substrate by applying external pressure where coverage of thiolate on the Au substrate at the contact areas between the roof and the substrate (the darker lines) was different from feature regions. The difference between these two regions could be eliminated by controlling the etching conditions, as demonstrated in Figs. 99.87(b) and 99.87(c).

The sizes of the trenches made from each stamp of line patterns are summarized in Table 99.V. For a stamp with a roof height of 1.3 $\mu$m, the generated trenches have widths of about 1/10 or slightly less than 1/10 of those on the original patterns, when the applied pressure was ~0.3 MPa. For instance, a trench width of ~1 $\mu$m was fabricated by using a 10 × 10-$\mu$m–sized line stamp. The percentage of size reduction did not change

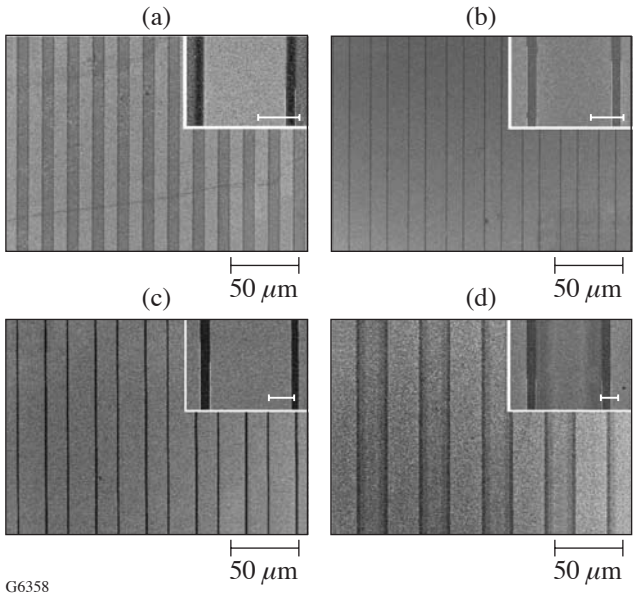


Figure 99.87
SEM images of trenches on surfaces of Au substrates fabricated using oCP from (a) 10 × 10-$\mu$m, (b) 15 × 15-$\mu$m, (c) 20 × 20-$\mu$m, and (d) 25 × 25-$\mu$m stamps. The scale bars in the insets are 5 $\mu$m.

Table 99.V: Dimensions and aspect ratios of the PDMS stamps of parallel lines used, the calculated minimum pressure for causing contacts between the roofs and substrates, the applied pressures, and the trench sizes fabricated in gold substrates using oCP.

| Width ($\mu$m) | | Height* $h$ ($\mu$m) | Aspect ratio ($h/w$) | $\sigma_{min}$** (MPa) | $\sigma_{applied}$ (MPa) | Trench size fabricated ($\mu$m) | | |
|---|---|---|---|---|---|---|---|---|
| Trench $2a$ | Feature $2w$ | | | | | Trench 1 | Trench 2 | Trench 3 |
| 10 | 10 | 1.30 | 0.13 | 0.13 | 0.3 | 0.99 | 1.09 | 1.0 |
| 15 | 15 | 1.30 | 0.087 | 0.87 | 0.3 | 1.01 | 1.30 | 1.2 |
| 20 | 20 | 1.30 | 0.065 | 0.065 | 0.3 | 1.48 | 1.80 | 1.6 |
| 25 | 25 | 1.30 | 0.052 | 0.052 | 0.3 | 2.31 | 2.32 | 2.3 |

*The height was estimated by AFM.
**Calculation was based on the equation given in the text.

substantially for patterns with line widths between 10 $\mu$m and 25 $\mu$m when the height of the roof was maintained the same and the features had height-to-width ratios varying between 0.052 and 0.13. All of these aspect ratios were smaller than the critical threshold value of 0.2 at which substantial external pressures is required to collapse the roof.[5] Our preliminary data indicate that the oCP technique can be extended to fabricate submicron and potentially nanometer-sized structures. Figure 99.88 shows an SEM image of submicron-sized trenches on the surface of the Au substrate fabricated from 1 × 1-$\mu$m line stamp with a height of ~0.5 $\mu$m using oCP technique. The average trench width was ~300 nm, although only a single trench per repeating unit has been produced. Careful design in stamp geometry is required for a systematic study in this size-reduced range.

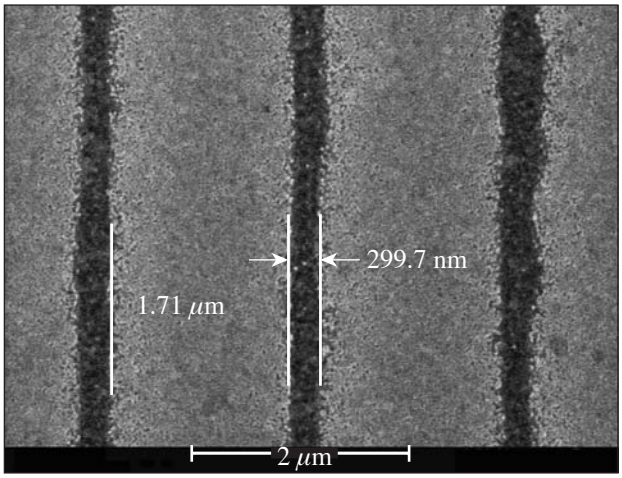


Figure 99.88
SEM image of submicron-sized trenches on the surface of Au substrate fabricated from 1 × 1-$\mu$m line stamps using oCP. Only a single trench per repeating unit has been produced.

The oCP technique was applied in patterning Pt@$Fe_2O_3$ core–shell nanoparticles to create anti-ring and ring structures. Langmuir films of ~4-nm Pt@$Fe_2O_3$ core–shell nanoparticles were transferred onto a PDMS stamp of well arrays (10 $\mu$m in well diameter with a well center-to-center distance of 15 $\mu$m). Overpressure and extended overpressure printing on plasma-cleaned Si substrates were used to obtain anti-ring and ring patterns, respectively. Figure 99.89 shows the SEM images of the single and arrays of fabricated anti-ring and ring patterns of Pt@$Fe_2O_3$ nanoparticles at different magnifications. The patterns were relatively uniform over a large area. The ring and anti-ring patterns obtained were not completely complimentary to each other. The average trench width of the anti-rings was ~1.3 $\mu$m, while the rings had an average line width of ~1.1 $\mu$m. Some of the rings were not completely closed loops or had variation in line width, which could be due to the rupture of the nanoparticulate films during contact printing. Similar defects at the inner and outer perimeters could be found for anti-ring patterns. This effect could be minimized by optimizing the thickness of the nanoparticulate films and using precise control in releasing the stamp.

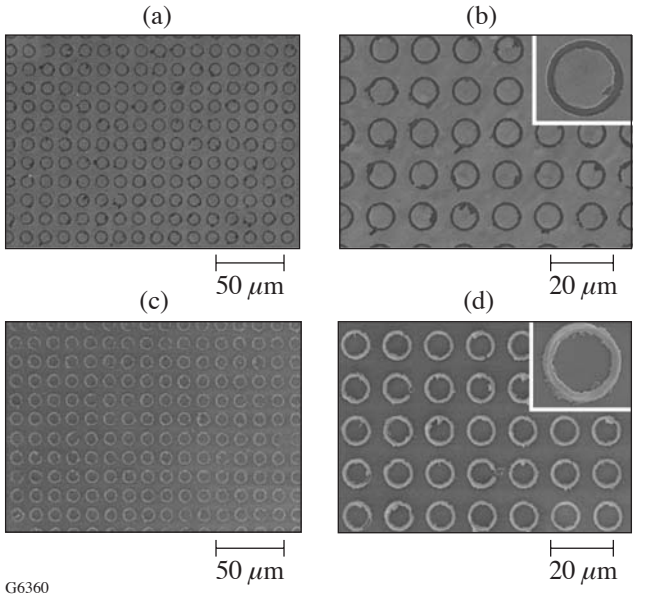


Figure 99.89
SEM images of [(a), (b)] anti-ring and [(c), (d)] ring patterns of Pt@$Fe_2O_3$ nanoparticles. Insets in (b) and (d) show the individual anti-ring and ring, respectively.

Tapping-mode AFM was used to examine the topology of the ring patterns made by extended oCP of Pt@$Fe_2O_3$ core–shell nanoparticles. Figures 99.90(a) and 99.90(b) show the three- (3-D) and two-dimensional (2-D) presentations of the ring structures of pLB films of Pt@$Fe_2O_3$ core–shell nanoparticles. The cross-section analysis shows that the rings had relatively uniform height [Fig. 99.90(c)]. The average height of the rings was ~285 nm, which corresponds to approximately 36 layers of nanoparticles. The number of layers in the rings was reasonable and further confirmed by measuring the height of six-layered unpatterned Pt@$Fe_2O_3$ nanoparticles to get an average thickness of a single particle layer. The AFM image and the cross-section analysis for an unpatterned six-layered film of Pt@$Fe_2O_3$ nanoparticles are shown in Fig. 99.91. The average thickness was 45 nm, which corresponds to a mono-

layer thickness of 7 to 8 nm. This value is reasonable since the 4-nm Pt@$Fe_2O_3$ core–shell nanoparticles are capped with oleic acid surfactants, which have a typical length of ~3 to 5 nm, depending on the configuration of hydrocarbon chains. The ruptured features observed in SEM were seen in the AFM image as well.

The patterned rings of Pt@$Fe_2O_3$ core–shell nanoparticles could be readily converted to face-centered tetragonal (fct) FePt alloy rings by thermal annealing in an atmosphere of 5% (*v*/*v*) hydrogen in argon at 450°C for 30 min.[15–19] Figures 99.92(a)–99.92(c) show the tapping-mode AFM images in 3-D and 2-D views and a cross-section analysis of the rings after the solid-state conversion. The average height of the patterns after annealing was approximately 140 nm. This value is reasonable considering the carbonization of surfactants and coalescence of nanoparticles upon annealing. The six-layered unpatterned film after the conversion had an average height of ~23 nm. Although the rings showed a large degree of shrinkage in height after the conversion, our cross-section analysis indicated that the line width of the ring did not show substantial broadening or shrinkage.

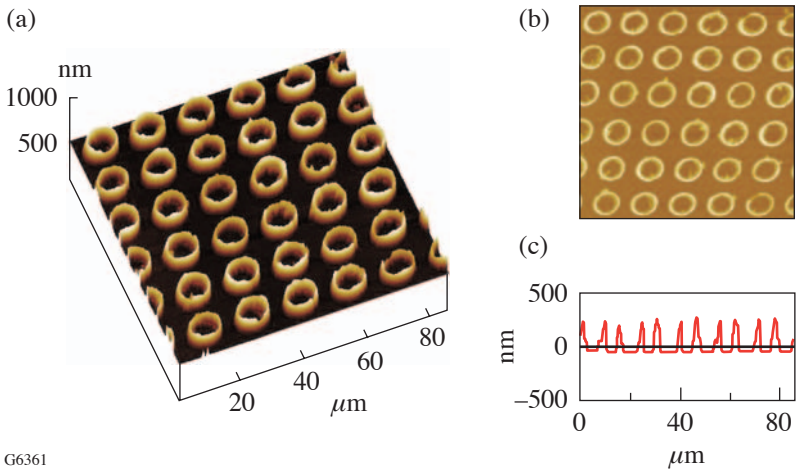


Figure 99.90
Tapping-mode AFM images of ring arrays of Pt@$Fe_2O_3$ nanoparticles: (a) 3-D representation, (b) 2-D representation, and (c) a cross-section analysis.

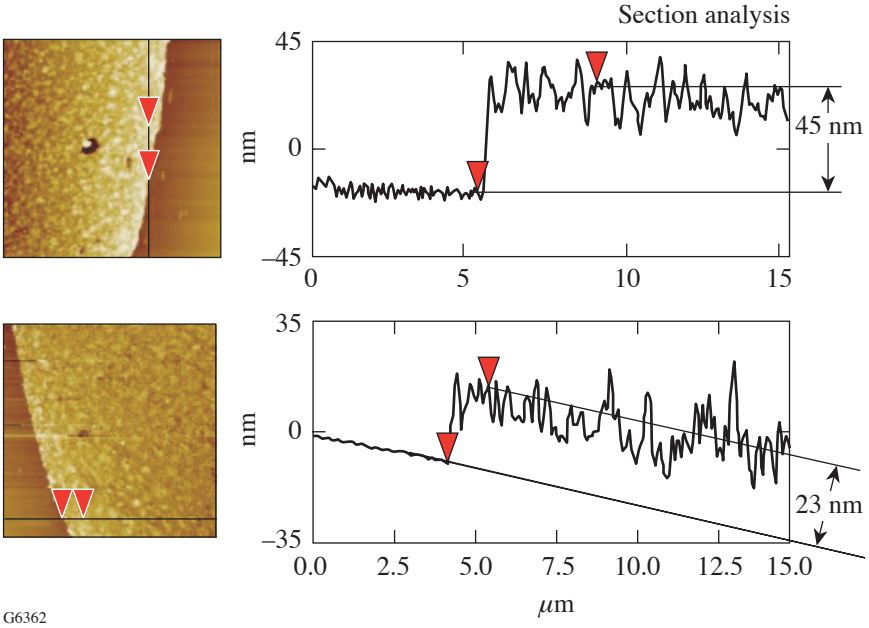


Figure 99.91
AFM images and their section analyses of six-layered unpatterned LB films of Pt@$Fe_2O_3$ core–shell nanoparticles (a) before and (b) after solid-state conversion.

MFM is a powerful tool to study magnetic properties of patterned structures.[20] In this technique, the topography contrast and magnetic interaction can be effectively separated by using tapping mode. As illustrated in Fig. 99.93(a), the phase contrast in an MFM image depends on the interaction of magnetic dipoles between the MFM tip coating layer and those of the substrate. Both low and high phase signals are possible for magnetic components on a substrate in comparison to nonmagnetic regions. The dark contrast indicates the magnetic repulsion between the tip and substrate, while the light-contrast region shows the attractive interaction. A relatively thick film was desired to have strong-enough magnetic signals for MFM characterization. Figure 99.93(b) shows the MFM study on the magnetization of the ring arrays characterized in Fig. 99.92. Both the tip and the substrate of FePt-magnetic ring on silicon have been premagnetized using a magnet (~0.2 to 0.25 Tesla). The magnetic response from the ring could be clearly visualized in the MFM image. The dark contrast indicated that the magnetic layer on the tip and the ring patterns repelled each other, which suggests that they were magnetized in the same direction.

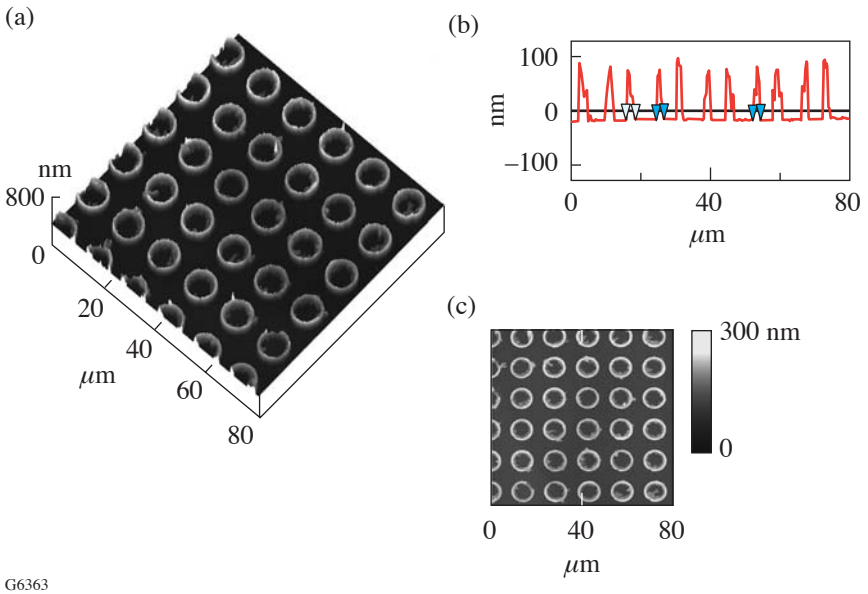


Figure 99.92
[(a)–(c)] Tapping-mode AFM images of FePt rings: (a) 3-D representation, (b) 2-D representation, and (c) cross-section analysis.

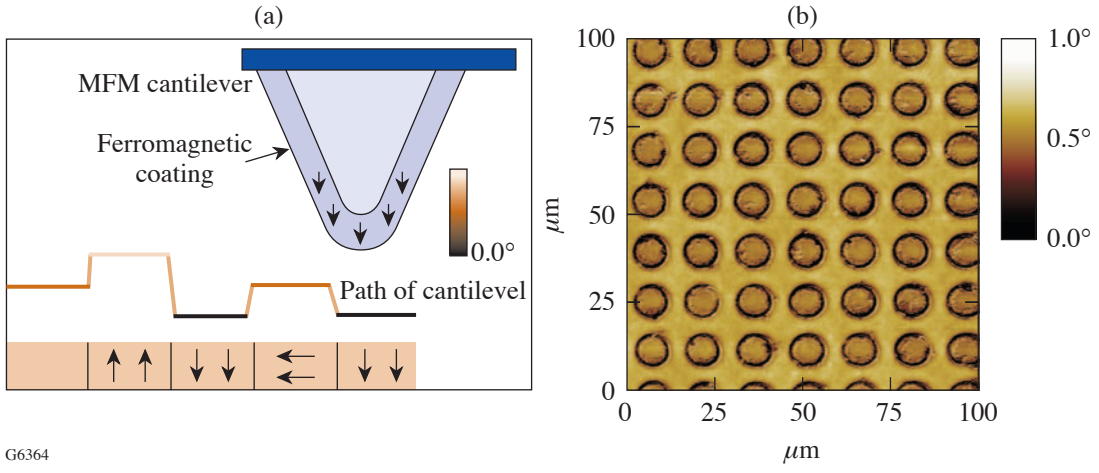


Figure 99.93
(a) An illustration of the magnetic interactions between MFM tip and patterned substrate and (b) MFM phase image of fct FePt magnetic rings made by extended oCP.

In conclusion, it has been demonstrated that a new patterning approach can be developed by controlling contact areas between the roof of an elastomeric stamp and the substrate surface to create size-reduced patterns. This technique is unique in that it offers a tool for making new patterns that may not exist on the original masters. The method is versatile and used to pattern self-assembled monolayers as well as thin films of nanoparticles. Fabrication of submicron-sized patterns is feasible with properly designed elastomeric stamps. The magnetic rings and anti-ring structures could have various novel applications, such as the study of magnetization reversal,[21] metastable states of magnetic rings,[12,22–24] and ring-based magnetic biological separations and manipulations.[25]

## ACKNOWLEDGMENT

This work was supported by the National Science Foundation and the U.S Department of Energy (DOE, DE-FC52-92SF19460) through the Laboratory for Laser Energetics at University of Rochester. We thank Mr. Justin Jiang of Harvard University for the gold substrates and Dr. Semyon Papernov (AFM and MFM) and Mr. Brian McIntyre (SEM) for help. The support of DOE does not constitute an endorsement by the DOE of the views expressed in this article.

## REFERENCES

1. Y. Xia *et al.*, Chem. Rev. **99**, 1823 (1999).
2. Y. Xia and G. M. Whitesides, Angew. Chem., Int. Ed. Engl. **37**, 550 (1998).
3. B. D. Gates *et al.*, Annu. Rev. Mater. Res. **34**, 339 (2004).
4. Y. Xia and G. M. Whitesides, Langmuir **13**, 2059 (1997).
5. E. Delamarche *et al.*, Adv. Mater. **9**, 741 (1997).
6. D. Armani, C. Liu, and N. Aluru, in *Twelfth IEEE International Conference on Micro Electro Mechanical Systems* (IEEE, Orlando, FL, 1999), pp. 222–227.
7. A. Bietsch and B. Michel, J. Appl. Phys. **88**, 4310 (2000).
8. C. Y. Hui *et al.*, Langmuir **18**, 1394 (2002).
9. J.-G. Zhu, Y. Zheng, and G. A. Prinz, J. Appl. Phys. **87**, 6668 (2000).
10. Y. Chen *et al.*, Microelectron. Eng. **57–58**, 405 (2001).
11. L. J. Heyderman *et al.*, J. Appl. Phys. **93**, 10,011 (2003).
12. F. J. Castaño *et al.*, Phys. Rev. B, Condens. Matter **67**, 184425 (2003).
13. S. B. Clendenning *et al.*, J. Mater. Chem. **14**, 1686 (2004).
14. Q. Guo *et al.*, J. Am. Chem. Soc. **125**, 630 (2003).
15. Q. Guo, X. Teng, and H. Yang, Adv. Mater. **16**, 1337 (2004).
16. H. Yang *et al.*, Adv. Mater. **13**, 54 (2001).
17. X. Teng and H. Yang, J. Mater. Chem. **14**, 774 (2004).
18. X. Teng *et al.*, Nano Lett. **3**, 261 (2003).
19. X. Teng and H. Yang, J. Am. Chem. Soc. **125**, 14,559 (2003).
20. X. Zhu and P. Grütter, MRS Bull. **29**, 457 (2004).
21. S. P. Li *et al.*, Phys. Rev. Lett. **86**, 1102 (2001).
22. M. Kläui *et al.*, Appl. Phys. Lett. **78**, 3268 (2001).
23. M. Kläui *et al.*, Appl. Phys. Lett. **84**, 951 (2004).
24. M. Steiner and J. Nitta, Appl. Phys. Lett. **84**, 939 (2004).
25. H. Lee *et al.*, Nano Lett. **4**, 995 (2004).